Research Article

Irfan Ullah*, Muhammad Faisal Javed, Deema Mohammed Alsekait, Mohammed Jameel, Hisham Alabduljabbar, Khawaja Atif Naseem and Diaa Salama AbdElminaam

Advanced hybrid machine learning models for estimating chloride penetration resistance of concrete structures for durability assessment: optimization and hyperparameter tuning

https://doi.org/10.1515/rams-2025-0186
Received April 9, 2025; accepted November 18, 2025;
published online December 17, 2025

Abstract: This study explored advanced hybrid machine learning (ML) techniques for estimating the non-steady-state migration coefficient (D_{nssm}) of concrete, a key indicator of chloride penetration resistance. Support vector regression (SVR) was integrated with four metaheuristic optimization techniques: grey wolf optimization (GWO), gorilla troops optimization (GTO), firefly algorithm (FFA), and particle swarm optimization (PSO) to improve predictive accuracy. Among these models, SVR-GTO exhibited the superior effectiveness, attaining the maximum R^2 of 0.97 and the lowest root mean square error (RMSE) of 0.93. The SVR-GWO model similarly demonstrated the robust predictive accuracy, with an R^2 of 0.92 and an RMSE of 1.55, whereas the SVR-PSO and SVR-FFA models recorded slightly lower R^2 of 0.91 and 0.89, with RMSE of 1.67 and 2.13, respectively. To enhance model transparency and interpretability, the study employs SHapley Additive exPlanations (SHAP), partial dependence plots, and individual conditional expectation plots, offering a comprehensive understanding of how predictors affect the predicted outcomes. SHAP model revealed the higher significance of water-to-binder ratio (W/B), migration test (MT) age, and total aggregate (TA) in predicting the D_{nssm}. An interactive graphical interface was created to estimate the D_{nssm} of concrete, allowing efficient model interaction and eliminating the need for physical experimentation.

Keywords: hybrid machine learning; concrete durability; chloride resistance

***Corresponding author: Irfan Ullah**, College of Civil and Transportation Engineering, Hohai University, Nanjing, China,
E-mail: 19pwciv5205@uetpeshawar.edu.pk
Muhammad Faisal Javed, Department of Civil Engineering, GIK Institute of Engineering Sciences and Technology, Swabi, 823640, Pakistan,
E-mail: arbabfaisal@giki.edu.pk
Deema Mohammed Alsekait, Department of Information Technology, College of Computer and Information Sciences, Princess Nourah bint Abdulrahman University, Riyadh 11671, Saudi Arabia,
E-mail: Dmalsekait@pnu.edu.sa
Mohammed Jameel, Department of Civil Engineering, College of Engineering, King Khalid University, Asir, Abha, Saudi Arabia,
E-mail: jamoali@kku.edu.sa. https://orcid.org/0000-0001-5968-6623
Hisham Alabduljabbar, Department of Civil Engineering, College of Engineering in Al-Kharj, Prince Sattam Bin 14 Abdulaziz University, Al-Kharj 11942, Saudi Arabia, E-mail: h.alabduljabbar@psau.edu.sa
Khawaja Atif Naseem, Arkansas Department of Transportation, 10324 Interstate 30, Little Rock, AR 72209, USA, E-mail: khawaja-atif.naseem1@louisiana.edu
Diaa Salama AbdElminaam, Faculty of Computers and Artificial Intelligence, Benha University, Benha, Egypt; and Jadara Research Center, Jadara University, Irbid, 21110, Jordan,
E-mail: diaa.salama@miuegypt.edu.eg

1 Introduction

Steel-reinforced concrete structures in coastal environments often suffer deterioration due to exposure to aggressive chemical agents, including water [1, 2], carbon dioxide [2–7], sulphates [7–9], and especially chloride ions [10–12]. Chlorides are the primary cause of corrosion in steel reinforcement, resulting in reduced durability, cracking, spalling, and loss of strength in concrete structures [13, 14]. When chloride ions penetrate the concrete's pore system, they disrupt the protective oxide layer on steel reinforcement, initiating corrosion that can cause severe structural damage and significant economic costs [15]. Corrosion begins once the chloride concentration at the steel surface exceeds a critical threshold, with the time to onset influenced by the concrete's diffusion properties and the environmental exposure to chloride. High chloride levels, common in marine areas, accelerate deterioration and reduce concrete's load-bearing capacity. To protect structures, it is essential to use low-chloride materials, corrosion inhibitors, protective

coatings, and properly designed concrete mixes with sufficient reinforcement cover. Regular monitoring and maintenance are also necessary to ensure long-term durability [15, 16].

Marine aerosols, generated by sea surface bubbles and transported inland by wind, are the primary source of chloride ions that cause corrosion in coastal concrete structures [17]. Their concentration increases with wind speed [18], while deicing salts add to chloride exposure even far from roads and at high elevations globally [19]. Assessing chloride accumulation in offshore concrete is vital for durability evaluation, with field data informing accurate chloride ingress models [20]. Chloride penetration involves multiple transport mechanisms, mainly diffusion, modeled using Fick's second law, where the diffusion coefficient measures ion spread over time [21]. Rapid chloride migration tests offer quick assessment but may lack field accuracy, whereas wetting-drying and immersion tests provide realistic results but are time-consuming [22]. Designing durable concrete requires optimizing mixes for chloride resistance and minimal cement use, but verifying this through standard lab tests is slow and resource intensive. Therefore, fast, reliable, and comprehensive predictive methods are needed to estimate chloride penetration resistance efficiently, addressing the complexity of chloride transport in concrete.

Several research studies have explored the implementation of machine learning (ML) in estimating the properties of concrete, thereby eliminating the need for laborious and resource-intensive laboratory testing. Multi-objective optimization techniques combined with ML algorithms have been employed to enhance ingredient proportions for concrete mix design, which can be implemented at batching facilities to efficiently produce high-strength concrete before construction [23]. A hybrid backpropagation neural network (BPNN) model utilizing ReLU activation functions was created to forecast the shear strength of reinforced concrete beams, achieving an R^2 value of 0.924 and a mean squared error of 10.611 kN [24]. An optimized BPNN was also developed to estimate surface chloride infiltration in concrete exposed to marine conditions, outperforming conventional and advanced models with an R^2 value of 0.91 and offering faster, more efficient predictions [25]. To estimate surface chloride content in marine concrete, ML models such as support vector regression (SVR) and extreme gradient boosting (XGBoost) were trained on preprocessed data, with the ensemble model achieving superior accuracy (R^2 = 0.95) compared to the individual models [26]. AQ21 and WEKA, using the J48 algorithm, were employed to automate the classification of plain and CFBC fly ash-enhanced concrete, identifying materials with high chloride resistance [27]. An artificial neural network (ANN) model was also used to assess chloride diffusivity in high-performance concrete, showing high prediction accuracy when validated against experimental data [28]. Additionally, a metaheuristic algorithm was applied to enhance a BPNN model's performance in predicting chloride levels, surpassing traditional BPNN methods [29]. Utilizing observed data, another ANN model was employed to correlate input parameters with the depth of chloride ion penetration under drying–wetting cycles [30]. ANN and XGBoost have proven effective in accurately predicting the natural frequencies of functionally graded nanobeams [31]. Physics-informed recurrent neural networks have enhanced elastoplastic constitutive modeling by improving stability and extrapolation capabilities [32]. Hybrid metaheuristic-optimized neural networks have achieved superior accuracy in predicting concrete-reinforcement bond strength, outperforming traditional analytical models [33]. Additionally, hybrid approaches combining ML and finite element analysis have accelerated material parameter calibration, resulting in improved accuracy and reduced computational time [34]. Moreover, XGB excelled in predicting remediation outcomes, with Bayesian optimization boosting model performance and SHAP analysis offering interpretability [35].

This study tackles a critical issue by minimizing the dependence on labor-intensive and resource-demanding laboratory tests for assessing chloride diffusion in concrete through advanced ML techniques. By leveraging hybrid ML models, this research aims to develop a reliable predictive framework for estimating the non-steady-state migration diffusion coefficient (D_{nssm}) of concrete, a crucial parameter for ensuring the long-term performance of reinforced concrete structures subjected to chloride exposure. Support vector regression (SVR) was integrated with four metaheuristic optimization techniques: grey wolf optimization (GWO), gorilla troops optimization (GTO), firefly algorithm (FFA), and particle swarm optimization (PSO) to improve predictive accuracy. These algorithms were selected based on a combination of their diverse exploration-exploitation mechanisms, proven effectiveness in solving complex nonlinear problems, and their increasing adoption in civil engineering applications. GWO and PSO are well-established and widely used due to their robustness and global search capabilities, whereas FFA offers excellent local search refinement through its light-attraction mechanism. GTO, a relatively recent algorithm, was included for its innovative exploration strategy, inspired by the social behavior of gorillas, and represents a novel addition to the field. The combination of established and emerging algorithms aimed to balance innovation with

performance reliability in optimizing SVR parameters. To enhance model interpretability, tools such as SHapley Additive exPlanations (SHAP), partial dependence plots (PDP), and individual conditional expectation plots (ICE) were used, offering important understanding of how individual input variables influence predictions. Furthermore, an interactive graphical interface was created to facilitate the prediction of D_{nssm}, providing rapid results and eliminating the reliance on conventional experimental methods.

2 Methodology

2.1 Database overview

The database comprises 843 data points that capture D_{nssm} values across various types of concrete. This database is collected from two channels: i) academic research projects [36], and ii) publications in international journals [21, 27, 37–42]. The D_{nssm} values serve as indicators for evaluating concrete's ability to withstand chloride ion infiltration, as illustrated in Figure 1.

The dataset comprises diverse concrete classifications, including conventional, lightweight, enhanced-strength, advanced-performance, and self-consolidating concrete. These concrete mixes are characterized by eight attributes that detail the components and their proportions: water-to-binder ratio, quantities of binders (slag, cement, silica fume, lime filler, and fly ash) measured in kg/m^3, amounts of fine and coarse aggregates in kg/m^3, and levels of chemical additives (air-entraining agents, superplasticizers, and plasticizers) as a percentage of the binder's weight.

The database encompasses various cement varieties documented in diverse standards as experimental data has been gathered from numerous regions of the world. To ensure uniformity, all cement types are standardized based on the European standard EN 197-1. This standard classifies cement into 27 unique types, organized into five main categories, as depicted in Figure 2. Within the database, there are 15 cement types representing the four primary cement groups as illustrated in Figure 3. Around 57 % of the experiments conducted incorporate supplementary cementitious materials. The water-to-binder ratio spans from 0.19 to 0.65. Within the dataset, admixtures consist of numerous compounds, including superplasticizers containing polycarboxylate ether, naphthalene, melamine sulfonate, and lignosulfonate, as well as air-entraining agents composed of vinsol resin, synthetic surfactants, and fatty acid soap. The statistical distribution of the features is given in Table 1. Further, box plots of the features and D_{nssm} are depicted in Figure 4.

Correlation heatmaps were utilized to evaluate multicollinearity issues. In the Spearman correlation matrix (Figure 5), a notable correlation exists between D_{nssm} and the water-to-binder ratio (W/B), with a coefficient of 0.57. This correlation is followed by water (0.45), fine aggregate (FA, 0.12), and coarse aggregate (CA, 0.07). Additionally, there are negative correlations of −0.36, −0.32, −0.21, −0.14, −0.13, and −0.12 with silica fume (SF), migration test age (MT Age), slag, total aggregate (TA), superplasticizer (SP), and fine

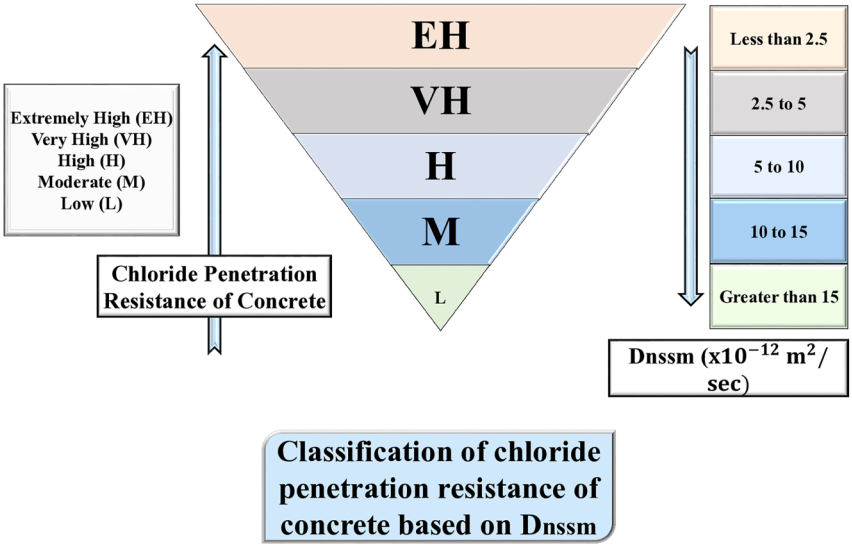

Figure 1: Chloride penetration resistance.

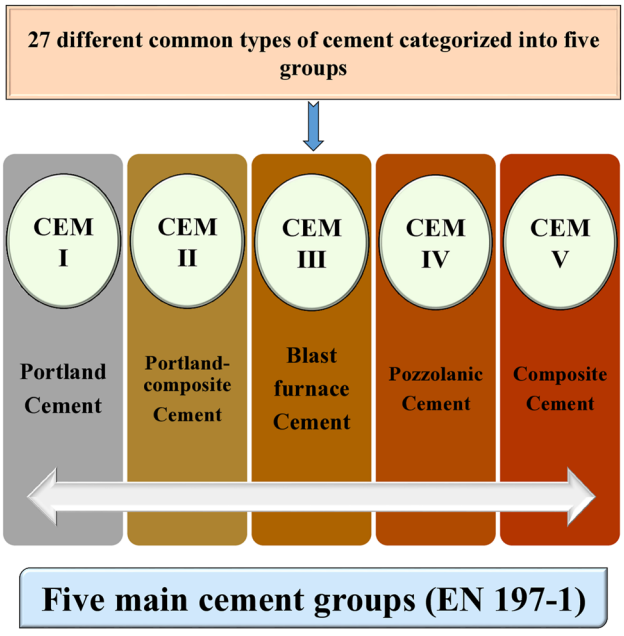

Figure 2: Cement groups (EN 197-1).

aggregate (FA), respectively. Likewise, in the Pearson correlation matrix (Figure 6), W/B exhibits the strongest linear association, with a correlation coefficient of 0.38, followed by CA (0.10) and TA (0.03). Conversely, there are negative correlations of −0.27 and −0.22 with SP and MT Age, respectively. As all features have correlation coefficients below 0.8, multicollinearity is not present.

2.2 Data preprocessing

The dataset consisted of 843 data points collected from academic journals and research projects, covering a wide range of concrete mixes. To ensure data quality, errors and duplicates were removed, and missing values were handled using manual and naïve imputation [43, 44]. Box plots were used to detect and remove outliers. Some features, like water, cement, and slag, had highly skewed distributions. Although log transformations were considered to correct this, standardizing the data with

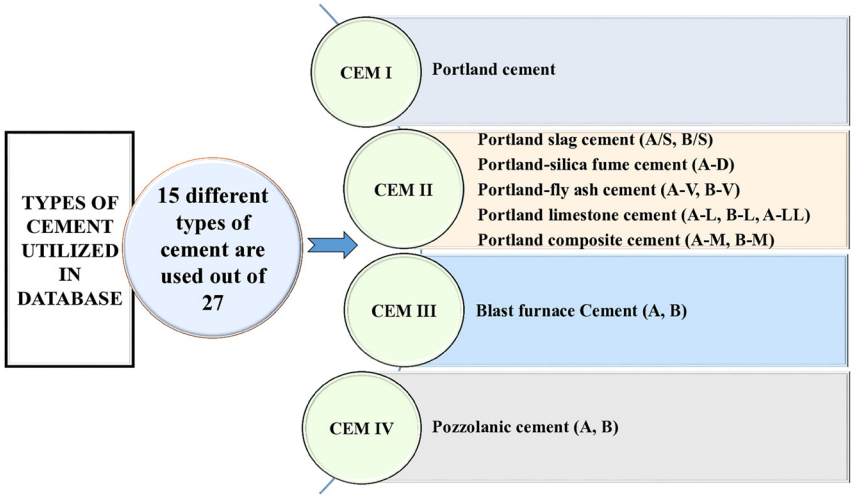

Figure 3: Cement types utilized in the database.

Table 1: Statistical intuitions into the features.

Statistics	W/B	Water kg/m^3	Cement kg/m^3	Slag kg/m^3	Fly ash kg/m^3	SF kg/m^3	FA kg/m^3	CA kg/m^3	TA kg/m^3	SP % (by W_b)	MT age Day	D_{nssm} ($\times 10^{-12}$ m^2/s)
Mean	0.42	162.3	330.07	29.3	33.9	5.28	759.06	818.5	1,636	0.48	83.06	9.1
Median	0.44	164.5	334.61	0	0	0	768	944	1746	0.47	28	7.04
Mode	0.45	162	360	0	0	0	786	463.0	1,960	0	28	8.8
SD	0.09	54.68	134.32	85.6	81.8	19.9	183.63	307.0	323.9	0.53	95.47	9.42
Maximum	0.65	1,049	2,384.97	1,284	735	468	1,574.1	1,240	2,097	4.17	365	133.6
Minimum	0.19	8.46	13.02	0	0	0	27.53	0	54.04	0	3	0.2
Skewness	−0.02	9.74	8.32	8.23	5.14	15.4	−0.47	−0.86	−2.33	1.25	1.83	5.4

SD, standard deviation.

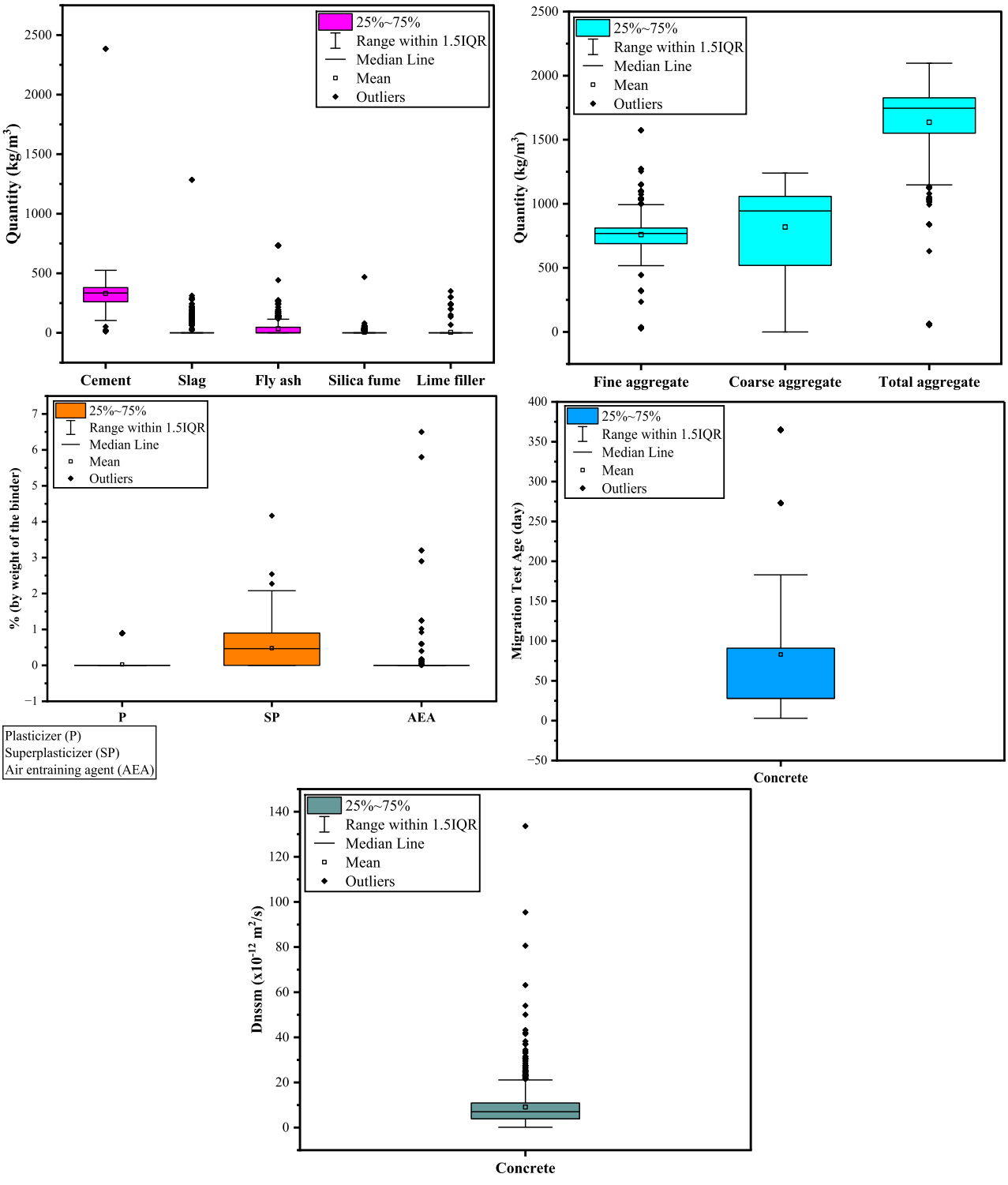

Figure 4: Statistical distribution of the features and label.

StandardScaler was enough to handle the skewness without changing the original meaning of the features.

All input features were scaled to have zero mean and unit variance to improve model stability and performance. Correlation analysis using Pearson and Spearman methods confirmed that all variables had correlation coefficients below 0.8, indicating low multicollinearity. The dataset had a high data-to-variable ratio (76.6), exceeding the

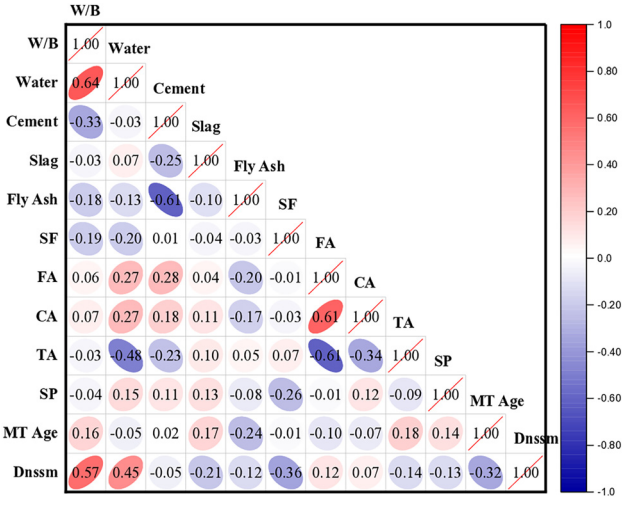

Figure 5: Spearman correlation heatmap.

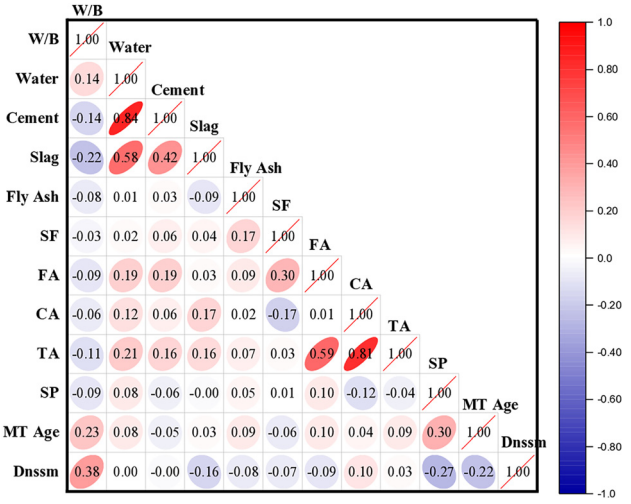

Figure 6: Pearson correlation heatmap.

recommended minimum and reducing the risk of overfitting [45, 46]. Additionally, 30 % of the data was reserved for testing and validation. For the hybrid models, parameter values for the metaheuristic algorithms (GWO, GTO, FFA, and PSO) were initially based on literature. A preliminary sensitivity analysis was also performed to fine-tune the parameters and ensure good optimization performance for the SVR models.

2.3 Model development

The optimization techniques PSO, GWO, FFA, and GTO were utilized to enhance the predictive performance of the SVR model in determining the D_{nssm}. An overview of the model development process is presented in Figure 7. The key SVR parameters include the radial basis function (RBF) kernel width (g) and penalty factor (C), each constrained within the range of 0.01–100. The parameter configurations for the ML models are as follows: In FFA, the absorption coefficient (α) is set to 0.2, the randomization parameter (rand) is 0.93, the initial attractiveness coefficient (β_0) is 2, and the light intensity absorption coefficient (γ) is 1. For GWO, the control variable (a) reduces in a linear fashion from an initial value of 2 down to 0. In PSO, the maximum velocity (V_{max}) is defined as 6, while the minimum (w_{min}) and maximum (w_{max}) inertia weights are 0.2 and 0.8, respectively. Additionally, the cognitive coefficient (c_1) and social coefficient (c_2) are assigned values of 1.6 and 1.8, respectively, to regulate swarm behaviour during optimization. The GTO algorithm utilizes 20 candidate solutions per iteration, with a maximum of 50 optimization iterations. A reproducibility seed of 42 ensures consistency in results, while the perturbation range is set at ±0.1. The candidate solution adjustment follows a random uniform perturbation mechanism based on both exploitation and exploration strategies. These optimized parameter settings enhance the efficiency of the SVR model in predicting the response parameter.

2.4 Assessment of model effectiveness

Every model is subjected to a comprehensive assessment procedure, which involves computing a range of performance indicators to evaluate its effectiveness (Figure 8). The mathematical formulations for these statistical indices are provided in Eqs. (1–6).

$$R^2 = \frac{\left[\sum_{i=1}^{i=n}\left(P_i - \overline{P}_i\right)\left(Q_i - \overline{Q}_i\right)\right]^2}{\sum_{i=1}^{i=n}\left(P_i - \overline{P}_i\right)^2 \sum_{i=1}^{i=n}\left(Q_i - \overline{Q}_i\right)^2} \tag{1}$$

$$\text{Adj}\, R^2 = 1 - \frac{\left(1 - R^2\right)(N-1)}{N - K_{n^{-1}}} \tag{2}$$

$$\text{RMSE} = \sqrt{\frac{1}{N}\sum_{i=1}^{i=n}\left(P_I - Q_i\right)^2} \tag{3}$$

$$\text{MAE} = \frac{1}{N}\sum_{i=1}^{i=n}\left|P_i - \text{Q}_i\right| \tag{4}$$

$$a10 - \text{index} = \frac{R10}{N} \tag{5}$$

$$a20 - \text{index} = \frac{R20}{N} \tag{6}$$

Where P_i depicts the actual value, while Q_i represents the

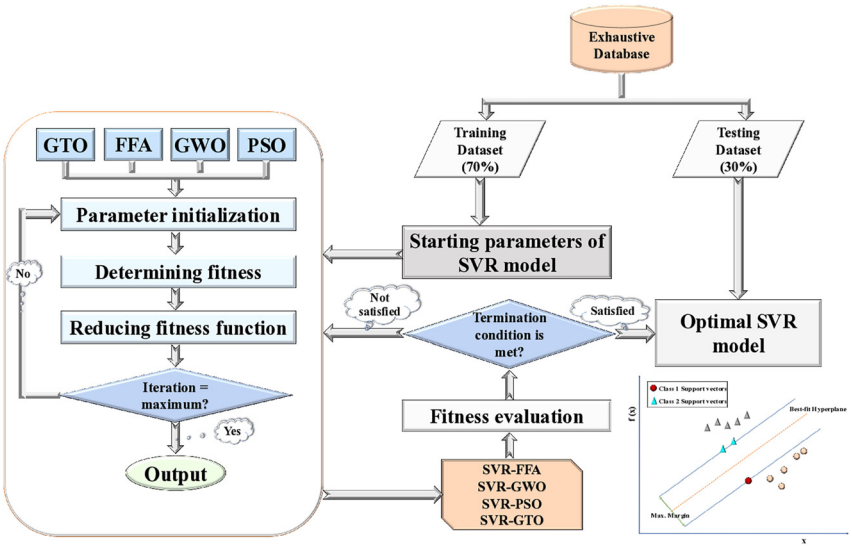

Figure 7: Overview of hybrid model development.

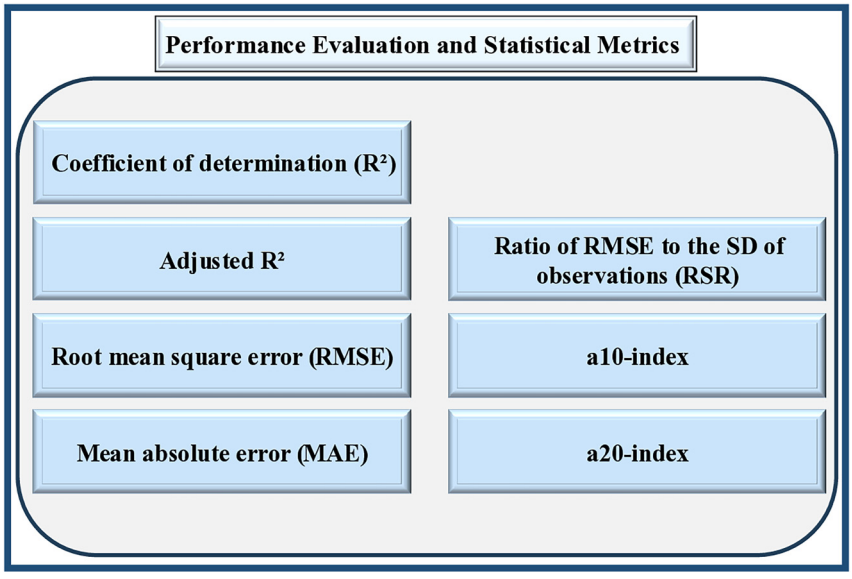

Figure 8: Performance indicators for assessing model efficacy.

anticipated value, where N refers to the total observations, and K_n represents the number of predictors. The letter with a bar on top represents the average values. $R20$ denotes the anticipated number of values falling within the ratio range of 0.90–1.20 for experimental-to-predicted values, whereas $R10$ represents the count of values within the range of 0.80–1.10.

3 Results and discussions

3.1 Performance analysis

Regression analysis is crucial for evaluating the predictive accuracy of ML models by quantifying the alignment between predicted and observed values (Figure 9). A regression coefficient close to 1, particularly above 0.8, demonstrates the model's effectiveness in capturing complex relationships [47, 48]. The obtained regression slopes validate the performance of the suggested SVR-based hybrid models (Figure 10). During the training phase, SVR-GTO exhibited the highest slope (0.93), followed by SVR-GWO (0.92), while SVR-PSO and SVR-FFA both achieved a slope of 0.85. In the testing phase, the regression slopes further improved, with SVR-GTO increasing to 0.96, SVR-GWO reaching 0.93, SVR-PSO attaining 0.91, and SVR-FFA maintaining a strong slope of 0.88. These results confirm the robustness of the models in estimating chloride penetration resistance in concrete, ensuring minimal deviation from experimental values and reinforcing their

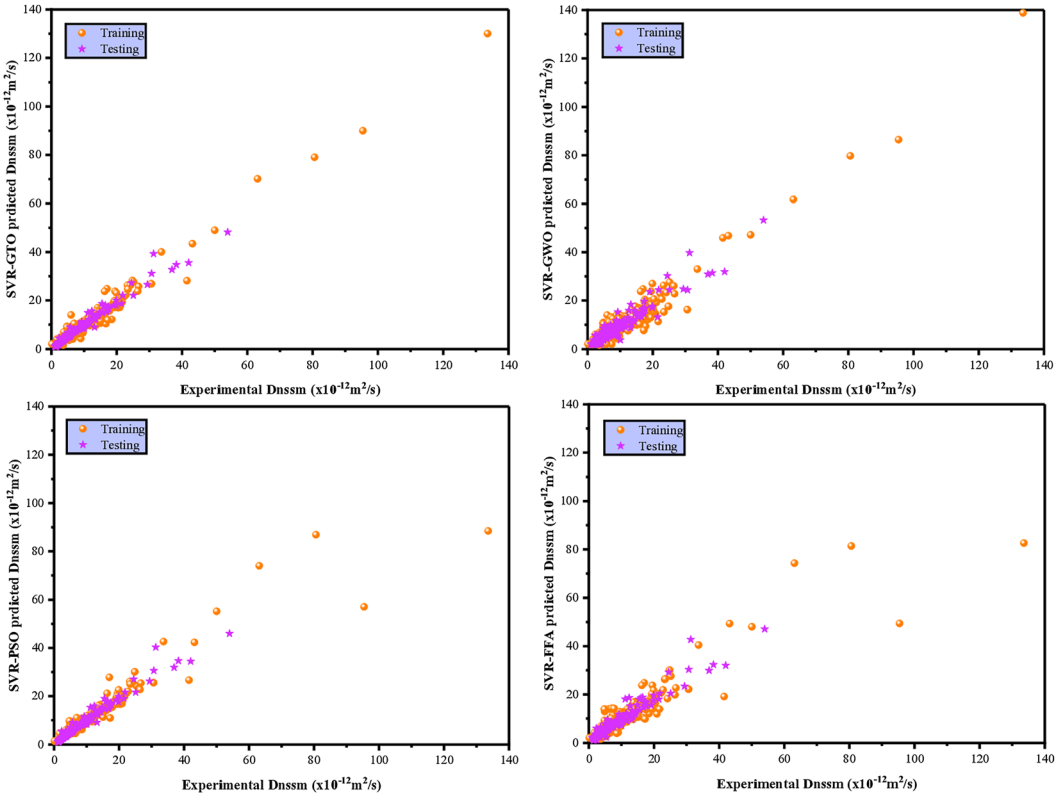

Figure 9: Scatter plots comparing predicted and actual values.

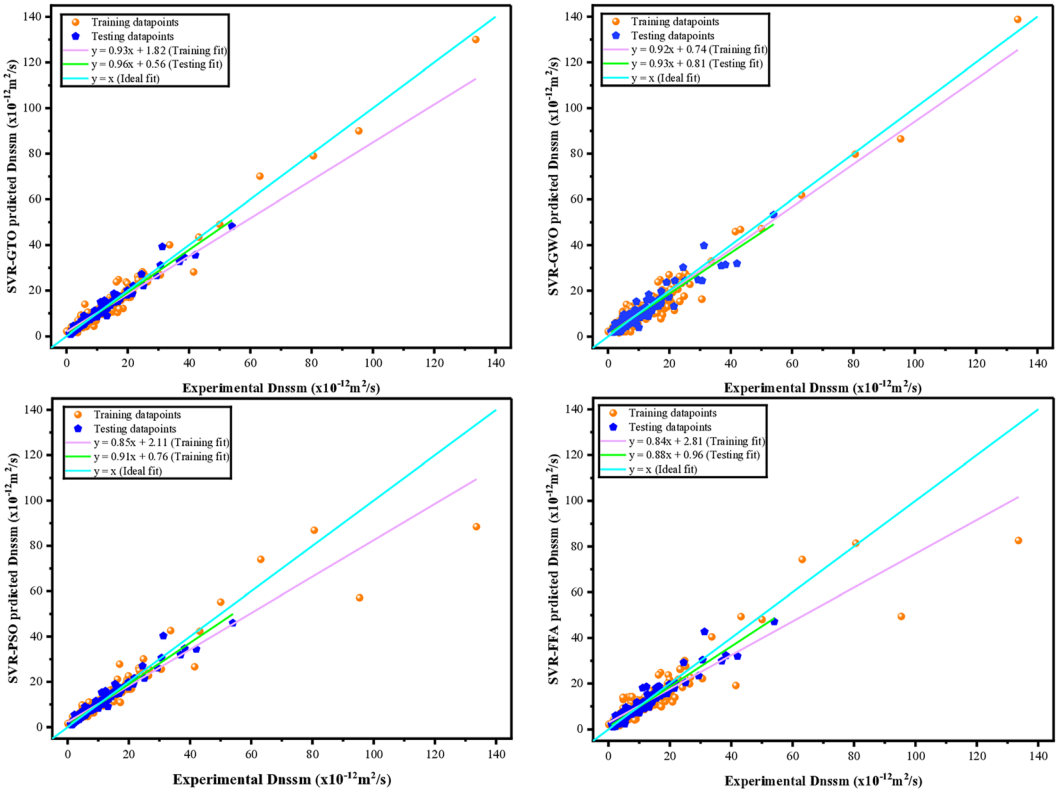

Figure 10: Regression analysis of the developed models.

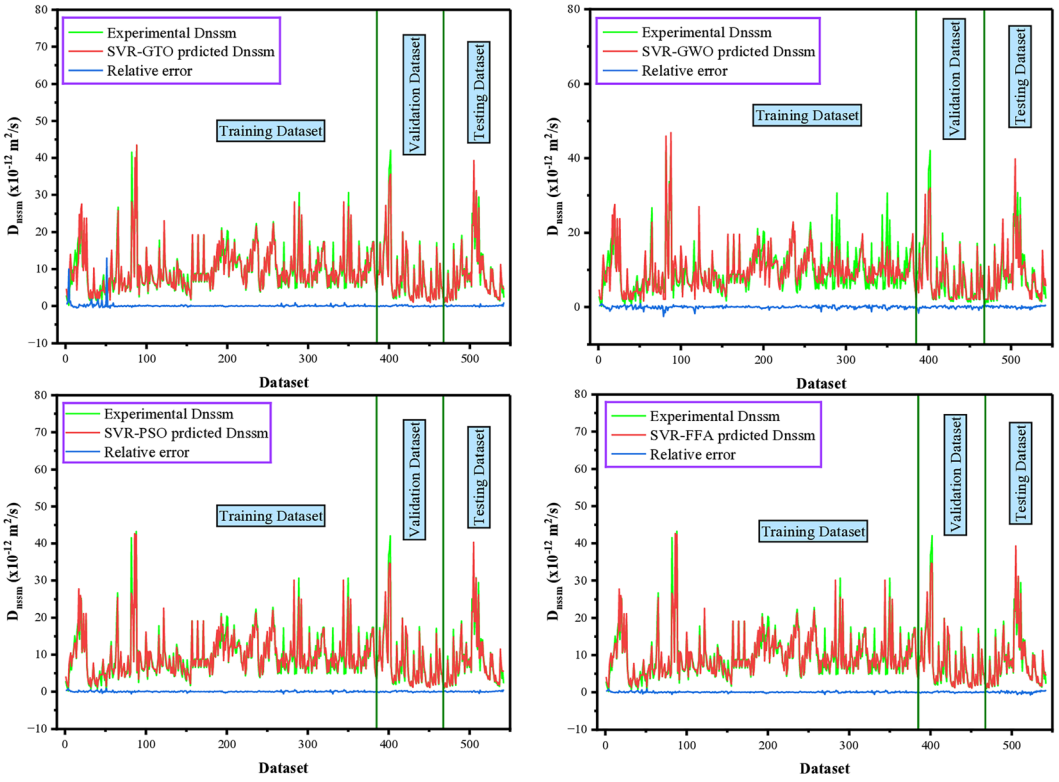

Figure 11: Evaluation of prediction accuracy using actual, predicted, and relative error values.

applicability in engineering practices. Additionally, Figure 11 presents an evaluation of the prediction accuracy by comparing actual and predicted values, along with the corresponding relative errors.

3.2 Assessment of model effectiveness

The statistical assessment of the ML models was conducted utilizing key performance indicators for both the training and testing phases (Table 2). In the training phase, SVR-GTO achieved the highest accuracy with an R^2 of 0.95 and an RMSE of 2.95, followed closely by SVR-GWO (R^2 = 0.94, RMSE = 3.12). SVR-PSO and SVR-FFA demonstrated slightly lower performance, with R^2 values of 0.92 and 0.90, and RMSE values of 3.45 and 3.56, respectively.

In the testing phase, SVR-GTO again outperformed other models, attaining the highest R^2 of 0.97 and the lowest RMSE of 0.93, indicating strong generalization. SVR-GWO maintained solid performance (R^2 = 0.92, RMSE = 1.55), while SVR-PSO and SVR-FFA yielded R^2 values of 0.91 and 0.89, and RMSE values of 1.67 and 2.13,

Table 2: Overview of performance metrics for the proposed models.

Phase	Models	R^2	Adj R^2	RMSE	MAE	RSR	a-10 index	a-20 index
Training	SVR-GTO	0.95	0.95	2.95	1.13	0.25	0.94	0.97
	SVR-GWO	0.94	0.93	3.12	2.07	0.27	0.92	0.95
	SVR-PSO	0.92	0.91	3.45	2.21	0.33	0.91	0.93
	SVR-FFA	0.90	0.90	3.56	2.34	0.45	0.90	0.92
Testing	SVR-GTO	0.97	0.97	0.93	0.33	0.11	0.94	0.98
	SVR-GWO	0.92	0.92	1.55	0.69	0.19	0.92	0.94
	SVR-PSO	0.91	0.90	1.67	0.87	0.24	0.90	0.93
	SVR-FFA	0.89	0.90	2.13	1.12	0.43	0.89	0.91

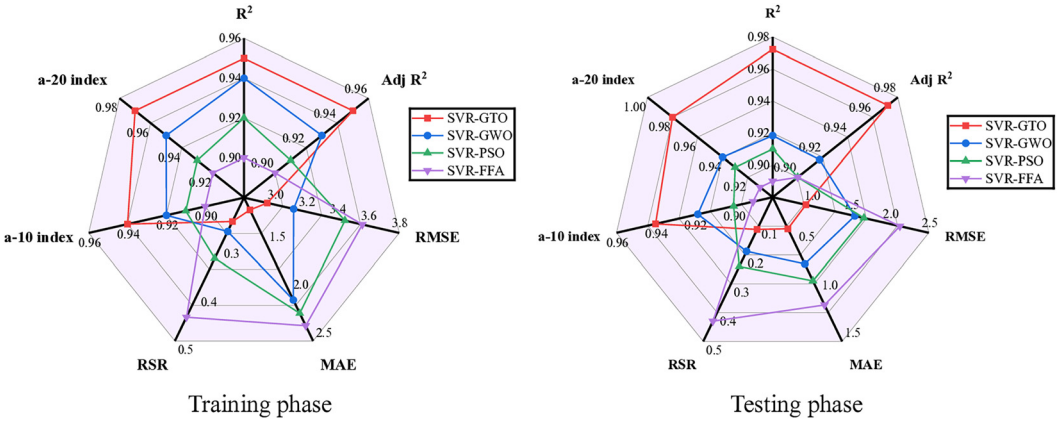

Figure 12: Spider plots of statistical indicator scores.

respectively. These findings confirm the superior accuracy and reliability of the SVR-GTO model in predicting chloride penetration resistance (Figure 12). The superior performance of SVR-GTO can be attributed to the unique exploration–exploitation balance of the GTO algorithm. GTO simulates the complex social behavior and dynamic movement patterns of gorilla troops, enabling it to effectively avoid local optima and explore the solution space more thoroughly. Its adaptive strategy and strong global search capability make it particularly suitable for high-dimensional, nonlinear problems such as predicting chloride diffusion in concrete.

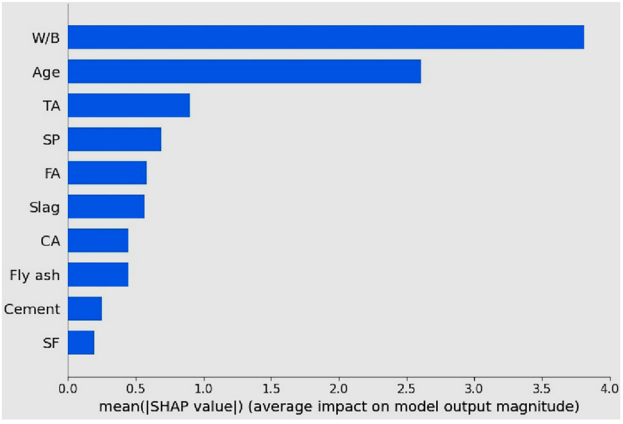

Figure 13: Mean SHAP plot: assessing feature's significance.

3.3 SHAP interpretation

The relative importance of input features in predicting D_{nssm} is illustrated in Figure 13 through SHAP analysis. The W/B exhibited the highest mean SHAP value (+3.8), underscoring its dominant influence on model predictions. MT Age followed with a mean value of +2.6, indicating its strong contribution to chloride resistance. TA and SP also demonstrated notable impacts, with SHAP values of +0.8 and slightly lower, respectively. Furthermore, fly ash and slag each contributed with a value of +0.6, while CA, cement, and SF showed smaller but meaningful effects, with SHAP values of 0.5, 0.3, and 0.2, respectively. These findings highlight the critical roles of mixture composition and curing age in determining chloride ingress behavior in concrete.

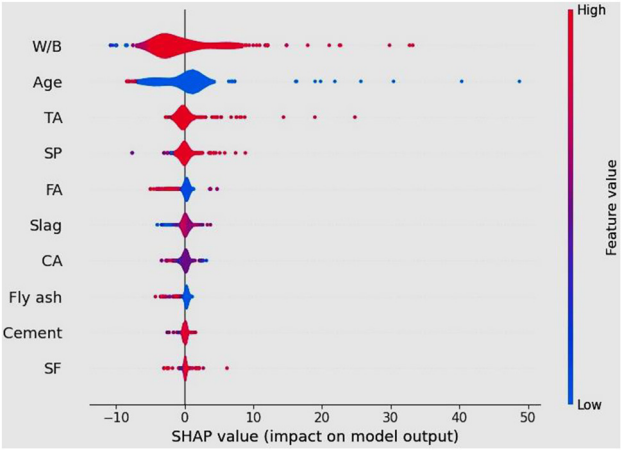

Figure 14: Impact of variables: SHAP summary visualization.

A rise in the W/B ratio is associated with a positive SHAP value of approximately +35, indicating that higher W/B ratios contribute positively to D_{nssm} (Figure 14). Conversely, a decrease in the W/B ratio depicts a negative SHAP value (around –10), suggesting a detrimental effect on D_{nssm}. The MT Age also plays a significant role, with higher durations showing negative SHAP values (around –8) and shorter durations exhibiting positive SHAP values (around +48). This implies that longer curing periods negatively impact D_{nssm},

while shorter durations have a positive influence. Similarly, higher FA quantities show negative SHAP values (−5), indicating adverse effects on D_{nssm} prediction, while lower FA amounts exhibit positive SHAP values (+3), implying beneficial impacts.

D_{nssm} shows contrasting trends with CA and TA content. Specifically, increasing CA content leads to a decrease in D_{nssm}, indicating improved resistance to chloride penetration. This occurs because larger, well-graded coarse aggregates disrupt the continuity of the cement paste, increasing the tortuosity of the diffusion path and effectively reducing the permeability of the concrete [49]. In contrast, while moderate increases in TA, which includes both fine and coarse aggregates, can improve the concrete matrix, very high TA levels lead to an increase in D_{nssm}. This rise may be attributed to the excessive volume of fine aggregates within the total aggregate fraction, which increases the interfacial transition zones (ITZs). Since ITZs are more porous than bulk paste, their expansion at very high TA contents can create easier pathways for chloride ions, thereby increasing chloride diffusivity. Hence, while coarse aggregate contributes positively to durability by blocking ion transport, an overly large total aggregate content, largely influenced by fine aggregate and the associated ITZ volume, can counteract this benefit and increase chloride permeability. This highlights the importance of optimizing both aggregate grading and overall aggregate volume to balance tortuosity effects with ITZ-induced permeability for enhanced concrete durability.

3.4 ICE and PDP interpretation

The D_{nssm} of concrete exhibits diverse trends across different material parameters (Figure 15). Initially, D_{nssm} increases with higher W/B ratios but only for a limited range, after which it stabilizes until approximately 0.44. Subsequently, there is a rapid increase in D_{nssm} from 0.44 to 0.49, maintaining a constant value up to 0.55. Similarly, D_{nssm} remains consistent up to 102 kg/m^3 of cement, beyond which it experiences a slight decrease until approximately 145 kg/m^3, remaining relatively constant thereafter.

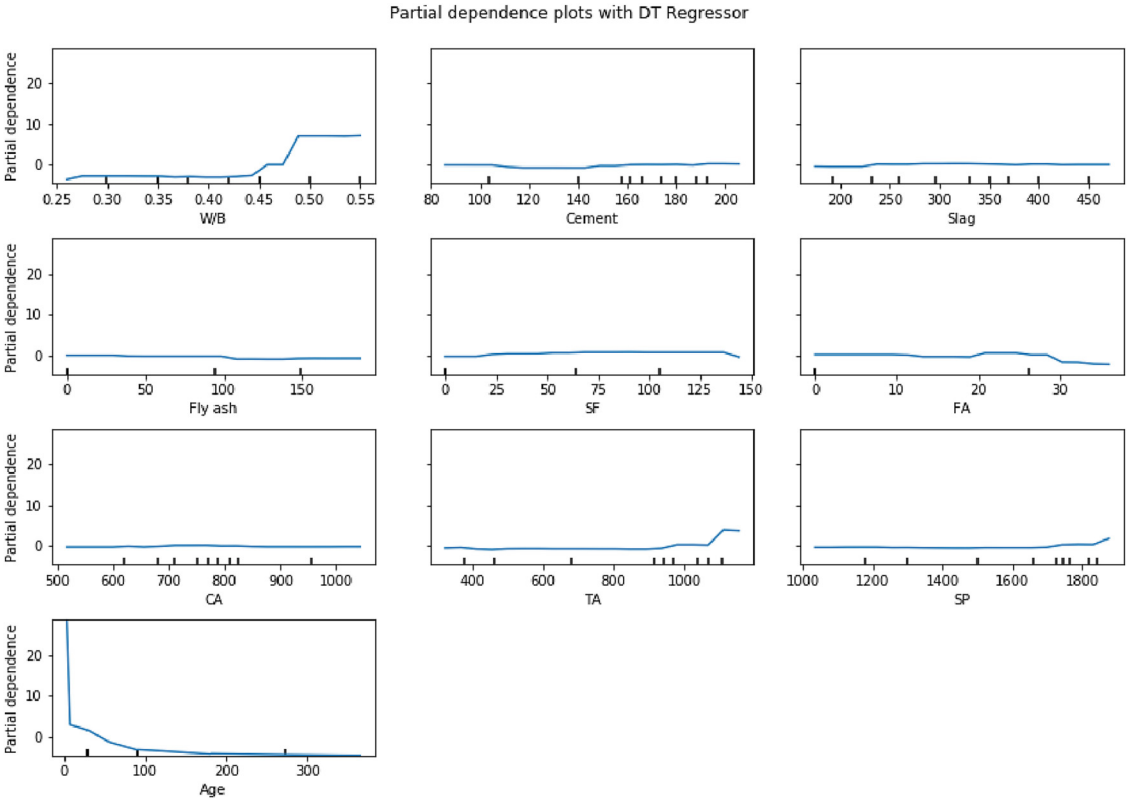

Figure 15: PDP analysis.

Additionally, D_{nssm} remains constant up to 225 kg/m^3 and then slightly decreases. Furthermore, D_{nssm} shows a slight decrease up to 90 kg/m^3, followed by a more significant decrease up to 100 kg/m^3, after which it remains constant. D_{nssm} almost remains constant with an increase in SF but decreases around 112 kg/m^3. It also decreases slightly up to 18 kg/m^{3}of FA, then shows a slight rise and decreases again. With an increase in CA content, D_{nssm} remains almost constant and slightly decreases initially but remains constant up to 980 kg/m^3, after which it increases. Moreover, D_{nssm} initially experiences a rapid fall with a rise in MT age and continues to decrease with further increases in MT age. The PDP analysis reveals that D_{nssm} rises sharply when the TA content exceeds approximately 1,100 kg/m^3, consistent with the SHAP findings.

The results of this study offer clear guidance for optimizing concrete mix designs to enhance durability against chloride ingress. Maintaining a low W/B ratio, ideally below 0.44, is a key factor in minimizing chloride diffusivity. A moderate cement content, around 102–145 kg/m^3, appears sufficient for maintaining strength without increasing permeability. Incorporating SF up to 112 kg/m^3 improves matrix densification, thereby reducing D_{nssm}. Increasing CA content up to 980 kg/m^3 is beneficial, as it enhances tortuosity and obstructs ion transport pathways. However, care must be taken with TA content. When TA exceeds 1,100 kg/m^3, D_{nssm} may increase due to a larger volume of ITZs, which are more porous and facilitate chloride movement. Additionally, extending the MT age shows that prolonged curing significantly improves chloride resistance. By carefully adjusting these key parameters, engineers can design concrete mixes with better long-term performance in chloride-rich environments.

Table 3: Comparative summary of ML models utilized in existing literature and the present study.

Reference	Best model	Model interpretation	R^2
[50]	XGBoost		0.99
[51]	PSO-XGBoost	SHAP	0.996
[52]	LGB		0.999
[53]	ANN	Sensitivity analysis	0.99
[54]	BR	SHAP	0.99
[55]	MLP		0.912
Current study	SVR-GTO	SHAP, ICE, and PDP	0.97

4 Comparison with existing models

ML has been increasingly integrated with analytical and numerical methods to enhance the prediction of complex structural behaviors and material properties. Among boosting algorithms used to predict the homogenized stiffness of fiber-reinforced composites, XGBoost achieved the highest accuracy [50]. For structural stability problems, a hybrid PSO-XGBoost model effectively estimated the buckling loads of columns with variable cross-sections, demonstrating near-perfect R^2 values and improved interpretability via SHAP analysis [51]. Similarly, ensemble models such as light gradient boosting (LGB) outperformed other techniques in predicting the buckling behavior of functionally graded nanobeams [52]. In concrete-related applications, ANN consistently exhibited superior predictive performance over traditional methods such as linear regression and decision trees [53]. Additionally, bagging regressors (BR) yielded the most accurate predictions in estimating wear depth in fly ash concrete [54]. For high-performance concrete, multilayer perception (MLP) showed superior predictive accuracy [55]. Table 3 presents a comparative summary of the models employed in previous literature and those adopted in the current study.

5 Graphical user interface (GUI)

An interactive GUI, depicted in Figure 17, was designed to streamline the prediction of the D_{nssm} of concrete. This innovative tool eliminates reliance on traditional labor-intensive laboratory testing, enabling rapid and accurate assessment of chloride penetration resistance. By inputting key parameters, users can efficiently obtain precise predictions of the migration coefficient, a critical indicator of concrete durability in chloride-exposed environments. The GUI, driven by advanced ML models, provides a practical and easy-to-use tool for researchers and professionals to

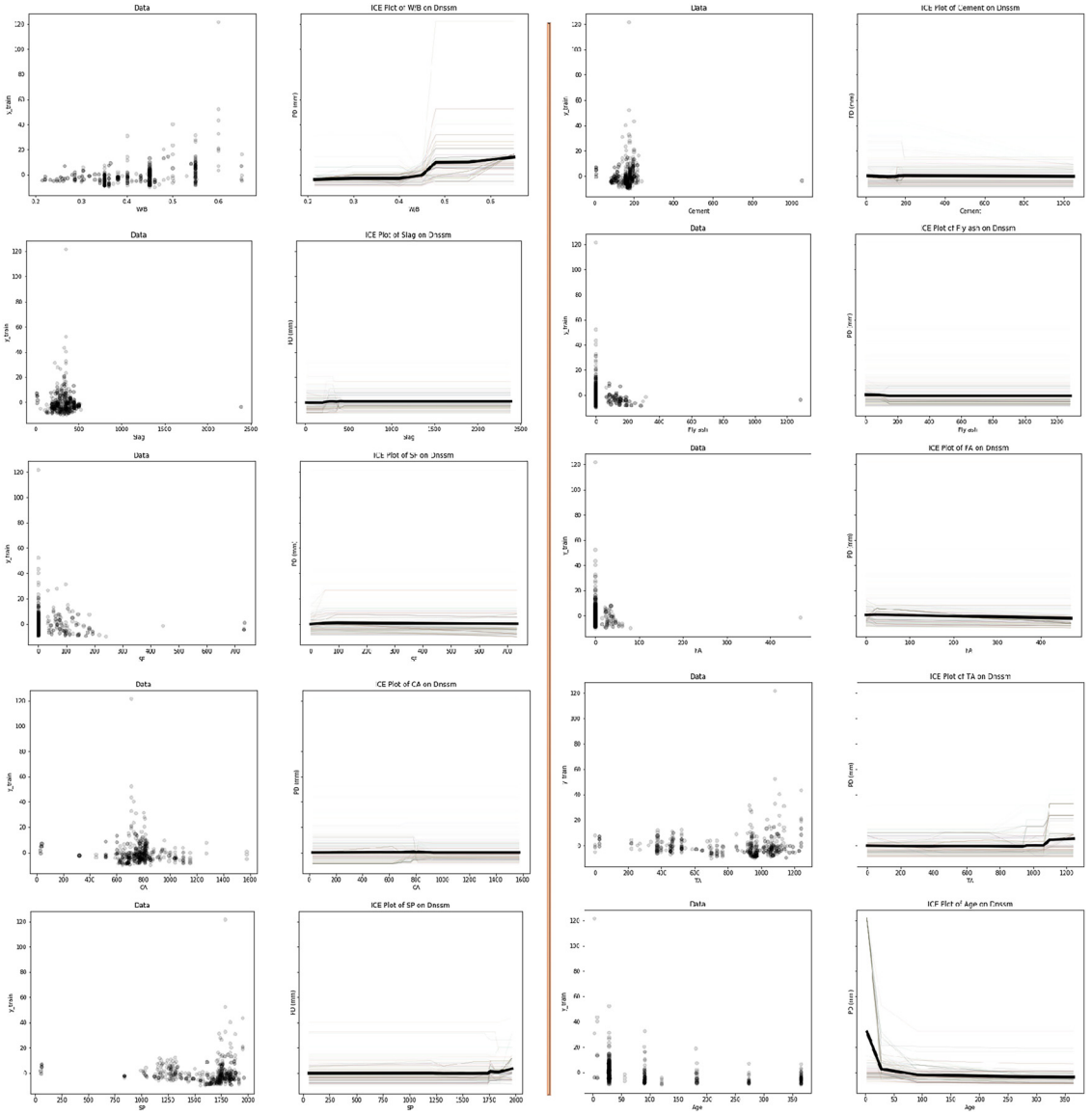

Figure 16: ICE analysis.

assess the durability of concrete structures. This interface represents a significant step forward in forecasting chloride resistance, supporting the development of long-lasting, resilient infrastructure in chloride-rich conditions (Figure 17).

6 Limitations and research directions for future

To make ML models more reliable, it is important to conduct experiments in controlled environments and collect data from a consistent, real-world source. This approach would improve dataset consistency and enhance the accuracy and reliability of ML models. The dataset, while comprehensive, may not fully represent all concrete types or environmental conditions, such as freeze-thaw cycles or varying chloride sources. This may limit the generalizability of the models to new scenarios. Additionally, future research should include additional predictors to assess the chloride resistance of concrete. For future research, deep learning techniques could be explored by expanding the dataset size to provide more comprehensive information, improving the model's generalization and predictive performance.

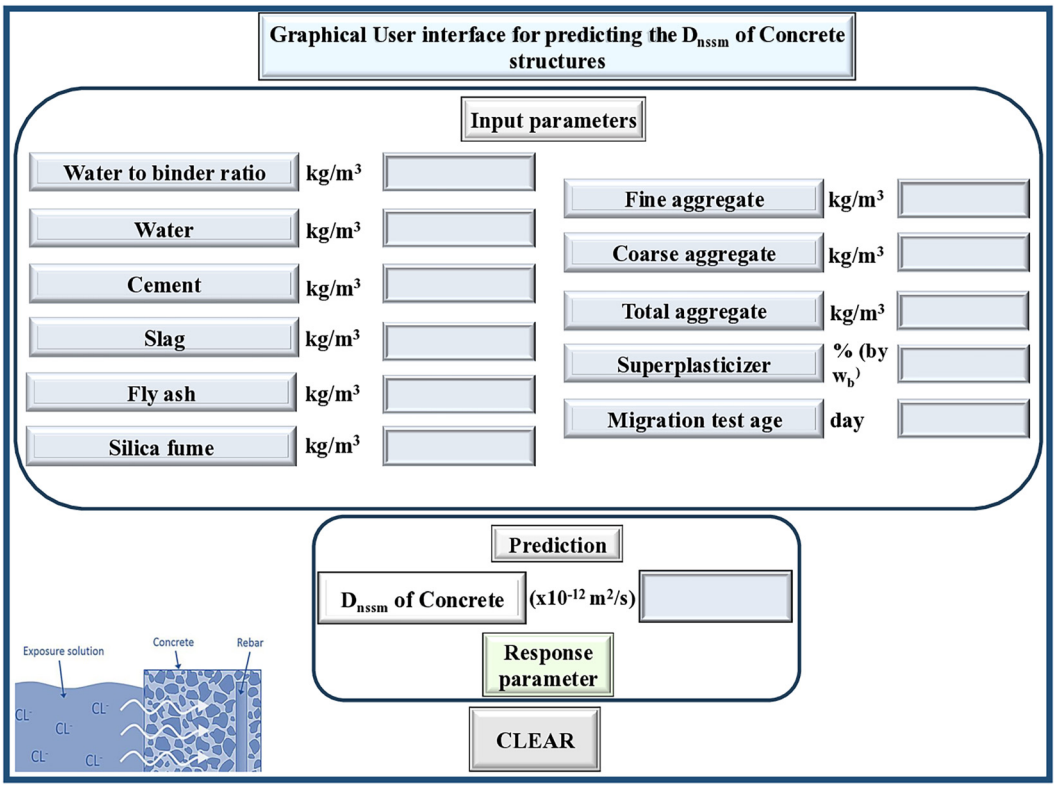

Figure 17: GUI

7 Conclusions

This study explored advanced hybrid ML techniques to predict the D_{nssm} of concrete, a key indicator of chloride penetration resistance. SVR was combined with four metaheuristic optimization algorithms: GTO, GWO, PSO, and FFA to enhance predictive accuracy. The primary outcomes of the study are succinctly outlined below:

- SVR-GTO attained the highest R^2 of 0.97 and the minimum RMSE of 0.93, demonstrating superior robustness and generalization capability, while SVR-GWO also exhibited strong predictive efficacy with an R^2 of 0.92 and an RMSE of 1.55; in comparison, SVR-PSO and SVR-FFA recorded slightly lower R^2 of 0.91 and 0.89, with RMSE values of 1.67 and 2.13, respectively.
- The analysis underscored the critical significance of the W/B ratio, MT Age, and TA in accurately estimating the chloride penetration resistance of concrete. Specifically, higher values of W/B and TA are associated with increased D_{nssm} values, indicating reduced chloride resistance in concrete. Conversely, greater MT Age corresponds to lower D_{nssm} values, signifying higher chloride resistance in concrete structures.
- A GUI was created to streamline the estimation of the D_{nssm} of concrete, eliminating the need for traditional, labor-intensive laboratory testing. The developed GUI, driven by advanced ML algorithms, provides a practical and easy-to-use tool for researchers and professionals to evaluate the durability of concrete structures.

Funding information: This research was funded by Princess Nourah bint Abdulrahman University Researchers Supporting Project number (PNURSP2025R435), Princess Nourah bint Abdulrahman University, Riyadh, Saudi Arabia.

Author contribution: All authors have accepted responsibility for the entire content of this manuscript and approved its submission.

Conflict of interest: The authors state no conflict of interest.

Data availability statement: The datasets generated and/or analysed during the current study are available from the corresponding author on reasonable request.

References

1. Liu J, Xing F, Dong B, Ma H, Pan D. Study on surface permeability of concrete under immersion. Materials (Basel) 2014;7:876–86.

2. Vicente C, Castela AS, Neves R, Montemor MF. Assessment of the influence of concrete modification in the water uptake/evaporation kinetics by electrochemical impedance spectroscopy. Electrochim Acta 2017;247:50–62.
3. Dong BQ, Qiu QW, Xiang JQ, Huang CJ, Xing F, Han NX, et al. Electrochemical impedance measurement and modeling analysis of the carbonation behavior for cementititous materials. Constr Build Mater 2014;54:558–65.
4. Dong B, Qiu Q, Gu Z, Xiang J, Huang C, Fang Y, et al. Characterization of carbonation behavior of fly ash blended cement materials by the electrochemical impedance spectroscopy method. Cem Concr Compos 2016;65:118–27.
5. Dong B, Qiu Q, Xiang J, Huang C, Xing F, Han N. Study on the carbonation behavior of cement mortar by electrochemical impedance spectroscopy. Materials (Basel) 2014;7:218–31.
6. Dong B, Qiu Q, Xiang J, Huang C, Sun H, Xing F, et al. Electrochemical impedance interpretation of the carbonation behavior for fly ash-slag-cement materials. Constr Build Mater 2015;93:933–42.
7. Qiu Q, Gu Z, Xiang J, Huang C, Hong S, Xing F, et al. Influence of slag incorporation on electrochemical behavior of carbonated cement. Constr Build Mater 2017;147:661–8.
8. Yu D, Guan B, He R, Xiong R, Liu Z. Sulfate attack of Portland cement concrete under dynamic flexural loading: a coupling function. Constr Build Mater 2016;115:478–85.
9. Gong J, Cao J, Wang YF. Effects of sulfate attack and dry-wet circulation on creep of fly-ash slag concrete. Constr Build Mater 2016;125:12–20.
10. Tang SW, Yao Y, Andrade C, Li ZJ. Recent durability studies on concrete structure. Cem Concr Res 2015;78:143–54.
11. Bernal J, Fenaux M, Moragues A, Reyes E, Gálvez JC. Study of chloride penetration in concretes exposed to high-mountain weather conditions with presence of deicing salts. Constr Build Mater 2016; 127:971–83.
12. Berrocal CG, Lundgren K, Löfgren I. Corrosion of steel bars embedded in fibre reinforced concrete under chloride attack: state of the art. Cem Concr Res 2016;80:69–85.
13. Liu J, Qiu Q, Chen X, Xing F, Han N, He Y, et al. Understanding the interacted mechanism between carbonation and chloride aerosol attack in ordinary Portland cement concrete. Cem Concr Res 2017;95:217–25.
14. Liu JC, Wang TJ, Sung LC, Kao PF, Yang TY, Hao WR, et al. Influenza vaccination reduces hemorrhagic stroke risk in patients with atrial fibrillation: a population-based cohort study. Int J Cardiol 2017;232:315–23.
15. Montemor MF, Simões AMP, Ferreira MGS. Chloride-induced corrosion on reinforcing steel: from the fundamentals to the monitoring techniques. Cem Concr Compos 2003;25:491–502.
16. Tadayon MH, Shekarchi M, Tadayon M. Long-term field study of chloride ingress in concretes containing pozzolans exposed to severe marine tidal zone. Constr Build Mater 2016;123:611–6.
17. Liu J, Ou G, Qiu Q, Xing F, Tang K, Zeng J. Atmospheric chloride deposition in field concrete at coastal region. Constr Build Mater 2018; 190:1015–22.
18. Fitzgerald JW. Marine aerosols: a review. Atmos Environ Part A, Gen Top 1991;25:533–45.
19. Houska C, Houska C. Deicing salt – recognizing the corrosion threat, TMR consulting. Pittsburgh, PA USA; 1990:1990 p.
20. Liu J, Ou G, Qiu Q, Chen X, Hong J, Xing F. Chloride transport and microstructure of concrete with/without fly ash under atmospheric chloride condition. Constr Build Mater 2017;146:493–501.
21. Pontes J, Bogas JA, Real S, Silva A. The rapid chloride migration test in assessing the chloride penetration resistance of normal and lightweight concrete. Appl Sci 2021;11:7251.
22. Ann KY, Ahn JH, Ryou JS. The importance of chloride content at the concrete surface in assessing the time to corrosion of steel in concrete structures. Constr Build Mater 2009;23:239–45.
23. Tipu RK, Panchal VR, Pandya KS. Multi-objective optimized high-strength concrete mix design using a hybrid machine learning and metaheuristic algorithm. Asian J Civ Eng 2023;24:849–67.
24. Kumar Tipu R, Batra V, Suman PKS, Panchal VR. Shear capacity prediction for FRCM-strengthened RC beams using hybrid ReLU-Activated BPNN model. Structures 2023;58:105432.
25. Tipu RK, Panchal VR, Pandya KS. Enhancing chloride concentration prediction in marine concrete using conjugate gradient-optimized backpropagation neural network. Asian J Civ Eng 2024;25:637–56.
26. Tipu RK, Batra V, Suman PVR, Pandya KS. Predictive modelling of surface chloride concentration in marine concrete structures: a comparative analysis of machine learning approaches. Asian J Civ Eng 2024;25:1443–65.
27. Marks M, Jóźwiak-NiedzWiedzka D, Glinicki MA. Automatic categorization of chloride migration into concrete modified with CFBC ash. Comput Concr 2012;9:375–87.
28. Hodhod OA, Ahmed HI. Developing an artificial neural network model to evaluate chloride diffusivity in high performance concrete. HBRC J 2013;9:15–21.
29. Yao L, Ren L, Gong G. Evaluation of chloride diffusion in concrete using PSO-BP and BP neural network. IOP Conf Ser Earth Environ Sci 2021; 687:012037.
30. Delgado JMPQ, Silva FAN, Azevedo AC, Silva DF, Campello RLB, Santos RL. Artificial neural networks to assess the useful life of reinforced concrete elements deteriorated by accelerated chloride tests. J Build Eng 2020;31:101445.
31. Tariq A, Uzun B, Akpınar M, Yaylı MÖ, Deliktaş B. Size dependent dynamics of a bi-directional functionally graded nanobeam via machine learning methods. Adv Nano Res 2025;18:33–52.
32. Lourenço R, Tariq A, Georgieva P, Andrade-Campos A, Deliktaş B. On the use of physics-based constraints and validation KPI for data-driven elastoplastic constitutive modelling. Comput Methods Appl Mech Eng 2025;437:117743.
33. Safaeian Hamzehkolaei N, Ghavaminejad S, Barkhordari MS. Predictive model of bond strength in reinforced concrete structures: a hybrid metaheuristic-optimized neural network approach. Int J Eng Trans B Appl. 2025;38:1190–212.
34. Tariq A, Deliktaş B. An inverse parameter identification in finite element problems using machine learning-aided optimization framework. Exp Mech 2025;65:325–49.
35. Barkhordari MS, Zhou N, Li K, Qi C. Interpretable machine learning for predicting heavy metal removal efficiency in electrokinetic soil remediation. J Environ Chem Eng 2024;12:114330.
36. Kuosa H. Concrete durability field testing — Field and laboratory results 2007–2010 in DuraInt-project. VTT Research Report VTT-R-00482-11; 2011:96 p.
37. Choi YC, Park B, Pang GS, Lee KM, Choi S. Modelling of chloride diffusivity in concrete considering effect of aggregates. Constr Build Mater 2017;136:81–7.
38. Sell Junior FK, Wally GB, Teixeira FR, Magalhães FC. Experimental assessment of accelerated test methods for determining chloride diffusion coefficient in concrete. Rev IBRACON Estruturas e Mater 2021; 14:e14407.
39. Elfmarkova V, Spiesz P, Brouwers HJH. Determination of the chloride diffusion coefficient in blended cement mortars. Cem Concr Res 2015; 78:190–9.

40. Audenaert K, Yuan Q, De Schutter G. On the time dependency of the chloride migration coefficient in concrete. Constr Build Mater 2010;24: 396–402.
41. Park JI, Lee KM, Kwon SO, Bae SH, Jung SH, Yoo SW. Diffusion decay coefficient for chloride ions of concrete containing mineral admixtures. Adv Mater Sci Eng 2016;2016:1–11.
42. Marks M, Glinicki MA, Gibas K. Prediction of the chloride resistance of concrete modified with high calcium fly ash using machine learning. Materials (Basel) 2015;8:8714–27.
43. Anas M, Khan M, Bilal H, Jadoon S, Khan MN. Fiber reinforced concrete: a review †. Eng Proc 2022;22:3.
44. Alyami M, Nassar RUD, Khan M, Hammad AW, Alabduljabbar H, Nawaz R, et al. Estimating compressive strength of concrete containing rice husk ash using interpretable machine learning-based models. Case Stud Constr Mater 2024;20:e02901.
45. Alyami M, Khan M, Fawad M, Nawaz R, Hammad AWA, Najeh T, et al. Predictive modeling for compressive strength of 3D printed fiber-reinforced concrete using machine learning algorithms. Case Stud Constr Mater 2024;20:e02728.
46. Alyousef R, Rehman MF, Khan M, Fawad M, Khan AU, Hassan AM, et al. Machine learning-driven predictive models for compressive strength of steel fiber reinforced concrete subjected to high temperatures. Case Stud Constr Mater 2023;19:e02418.
47. Khan M, Khan A, Khan AU, Shakeel M, Khan K, Alabduljabbar H, et al. Intelligent prediction modeling for flexural capacity of FRP-strengthened reinforced concrete beams using machine learning algorithms. Heliyon 2024;10:e23375.
48. Alabduljabbar H, Khan M, Awan HH, Eldin SM, Alyousef R, Mohamed AM. Predicting ultra-high-performance concrete compressive strength using gene expression programming method. Case Stud Constr Mater 2023;18:e02074.
49. Yang Q, Wu Y, Zhi P, Zhu P. Effect of micro-cracks on chloride ion diffusion in concrete based on stochastic aggregate approach. Buildings 2024;14:1353.
50. Tariq A, Polat A, Deliktaş B. Boosting machine learning algorithms for predicting the macroscopic material behavior of continuous fiber reinforced composite. J Reinf Plast Compos. 2024. https://doi.org/10.1177/07316844241292694.
51. Polat A, Tariq A, Okay F, Deliktaş B. Investigation of the critical buckling load of a column with linearly varying moment of inertia using analytical, numerical, and hybrid machine learning approaches. J Strain Anal Eng Des 2025;60:612–31.
52. Tariq A, Uzun B, Deliktaş B, Yaylı MÖ. An investigation on ensemble machine learning algorithms for nonlinear stability response of a two-dimensional FG nanobeam. J Braz Soc Mech Sci Eng 2024;46:556.
53. Mohammed A, Burhan L, Ghafor K, Sarwar W, Mahmood W. Artificial neural network (ANN), M5P-tree, and regression analyses to predict the early age compression strength of concrete modified with DBC-21 and VK-98 polymers. Neural Comput Appl 2021; 33:7851–73.
54. Khan M, Nassar RUD, Khan AU, Houda M, El Hachem C, Rasheed M, et al. Optimizing durability assessment: machine learning models for depth of wear of environmentally-friendly concrete. Results Eng 2023; 20:101625.
55. Shakr PN, Mohammed A, Hamad SM, Kurda R. Electrical resistivity-compressive strength predictions for normal strength concrete with waste steel slag as a coarse aggregate replacement using various analytical models. Constr Build Mater 2022;327:127008.